

Liu Liang  
Zhang Baoji  
Zhang Hao  
Tang Hailin  
Wang Weijie



<http://dx.doi.org/10.21278/brod74308>

ISSN 0007-215X  
eISSN 1845-5859

## Hydrodynamic performance optimization of marine propellers based on fluid-structure coupling

UDC 62-253.6:629.5.015.4  
Original scientific paper

### Summary

Fiber-reinforced composites offer the benefits of high strength, high stiffness, lightweight, superior damping performance, and great design capability when compared to metal. The rigidity characteristics of the composite laminate in different directions may be adjusted to meet the requirements of the application by using appropriate materials and arranging the lay-up sequence. As a result, the purpose of this work is to explore the influence of lay-up type on propeller performance in terms of both hydrodynamic and structural performance. A transient fluid-structure interaction (FSI) algorithm based on the finite element method (FEM) combined with the computational fluid dynamics (CFD) technique is developed and used for the analysis of composite propellers. The hydrodynamic performance of the propeller is compared to that of a metallic material. Propeller propulsion efficiency, structural deformation, equivalent stress, and damage performance of different lay-up options under three different operating situations are compared. In addition, it is presented a parametric optimization approach to get the most appropriate lay-up program for composite blades with the best hydrodynamic properties and structural performance.

*Key words: composite marine propeller; lay-up type; fluid-structure interaction; CFD/FEM*

### 1. Introduction

Over the past century, the rigidity and fixed geometry design of marine metal propellers has approached the limits of their performance [1,2]. The high designability of composites has led to their use as an alternative to metal alloys in the manufacture of marine propellers [3,4]. Compared to conventional metal structures, carbon fiber/glass fiber reinforced composite structures offer a higher strength-to-weight ratio, excellent corrosion endurance, as well as a high level of elasticity to extreme loads [5,6]. Vibration can be reduced and better performance can be achieved by changing the fiber orientation. However, the composite design process is complex and can degrade the strength and performance of the propeller if not handled properly [7,8].

The rotation of a composite propeller in water is a process of fluid-structure interaction, which means that the composite propeller is elastically deformed by hydrodynamic loads, and the deformation of the propeller blade produces new perturbations of the fluid in the vicinity of the propeller, which leads to changes in hydrodynamic performance. Hence, a fluid-structure coupling approach applicable to composite propeller performance forecasting is established in the present study. Several studies have been conducted on the effect of plastic distortion on the hydrodynamic properties of composite propellers, which are based on potential flow theory, for example, the boundary element method (BEM) [9,10] and the lifting surface approach [11,12]. However, for predicting propeller hydrodynamic performance, the discrepancy between prediction results utilizing potential flow analysis and the viscous flow approach is substantial [13]. Lee et al. [14] used the fluid-structure interaction (FSI) methods based on BEM-FEM and CFD-FEM to forecast the hydrodynamic properties of the KP458 propeller in open water, respectively. For the rigid propeller, both FSI methods could predict the hydrodynamic performance of the blade in open water well. However, for the composite propeller with large deformation, the difference between the prediction results using the BEM and the CFD solver is greater than that for the rigid propeller. In recent years, fluid-structure interaction methods based on a combination of the viscous flow theory CFD solver and FEM approaches have been commonly employed to explore the hydrodynamic and structural aspects of marine composites [15-18].

Marine composite propellers are composed of a laminated matrix and fiber layers. The propeller blade has a good bending-torsional coupling behavior through a reasonable arrangement of fiber orientation, which improves the hydrodynamic performance and structural properties of the blade. Lin et al. [19] used the lifting surface method combined with the FEM solver to forecast the hydrodynamic and structural properties of composite blade, and the genetic algorithm (GA) was used to determine the better lay-up order of the propellers, which finally obtained a composite propeller with better performance than the traditional metal propeller. On this basis, the fluid-solid coupling performance of the blade in equilibrium and nonequilibrium lay-up order was studied and discussed by Lin [20]. The results showed that the properties of composite propellers can be affected by an unbalanced lay-up sequence, especially at low propulsion coefficients. In addition to the lay-up order, the properties of composite propellers are influenced by other factors, such as material properties and the environment in which the propeller operates. Zhang et al. [21] investigated the influence of the elastic modulus and the shear modulus on the hydrodynamic properties and structural deformation of the composite blade using a combination of CFD and FEM, which did not consider the combined effects of material properties and lay-up direction simultaneously. As a result, the impacts of lay-up order and material characteristics on composite propeller properties are illustrated in this study.

In this study, a transient bi-directional FSI methodology based on a combined CFD method and FEM is established and validated by numerical simulations. After that, finite element models of various composite blade structures are constructed, which have a variety of material properties and different lay-up sequences. Based on this, the hydrodynamic properties and structural properties under various materials, various lay-up sequences, and various operating conditions of the composite blade are compared. Finally, the parameter optimal approach is applied to determine the most appropriate lay-up scheme to realize the best equilibrium of hydrodynamic properties and structural properties of the composite blade.

## 2. Methodology and modeling setup

### 2.1 Geometry

In this paper, the KP458 standard propeller is selected for the numerical simulation of fluid-structure coupling, and the geometric model is given in Fig. 1. The KP458 is the backup propeller for the pool test of the KVLCC2 tanker, and the model was tested in the NMRI pool in open water. KRISO provides the detailed parameters of the KP458 propeller in Table 1.

**Table 1** Geometrical particulars of the KP458 model.

Project	Scale Ratio	Diameter (m)	$d/D$	$P/D$	$A_E/A_O$	No. of Blades	Angle of skew	Section Name
Value	1:58	0.17	0.155	0.721	0.431	4	21.15	NACA66

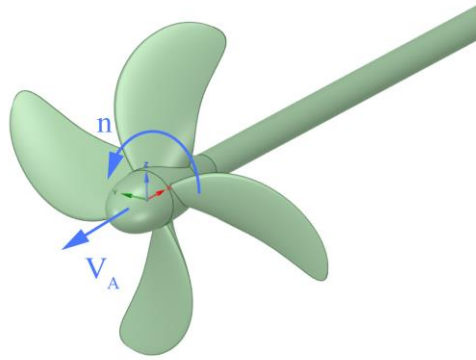


**Fig. 1** Geometrical model of KP458 propeller.

### 2.2 Fluid model and CFD setup

In the numerical simulation of fluid-structure coupling, the fluid around the propeller is assumed to be viscous and non-compressible. Based on this assumption, the hydrodynamic performance of the blade may be calculated by constructing the RANS equation, which can be expressed in tensor form as:

$$\frac{\partial u_i}{\partial x_i} = 0 \quad (1)$$

$$\rho \frac{\partial u_i}{\partial t} + \rho \frac{\partial u_i u_j}{\partial x_j} = -\frac{\partial p}{\partial x_i} + \frac{\partial}{\partial x_i} \left( \mu \frac{\partial u_i}{\partial x_j} - \overline{\rho u_i u_j} \right) + \rho f_i \quad (2)$$

where  $u_i$  and  $u_j$  are corresponding velocity components ( $i, j = 1, 2, 3$ );  $\rho$ ,  $p$ ,  $\mu$ ,  $f_i$ , and  $\overline{\rho u_i u_j}$  are the fluid density, the time-averaged value of pressure, dynamic viscosity coefficient of fluid, mass force, and Reynolds stress term, respectively.

To accurately simulate the revolution of the blade in the water, the whole flow domain consists of two parts which are the stationary region and the rotational region. The diameter of the stationary domain is  $6D$ , the distance of the inlet boundary from the blade is  $4D$ , the distance of the outlet boundary from the blade is  $8D$ , and the diameter of the rotating domain is  $1.2D$ . Interfaces are generated between the static and rotating regions through a shared topology for data transfer. The flow field computational region is shown in Fig. 2.

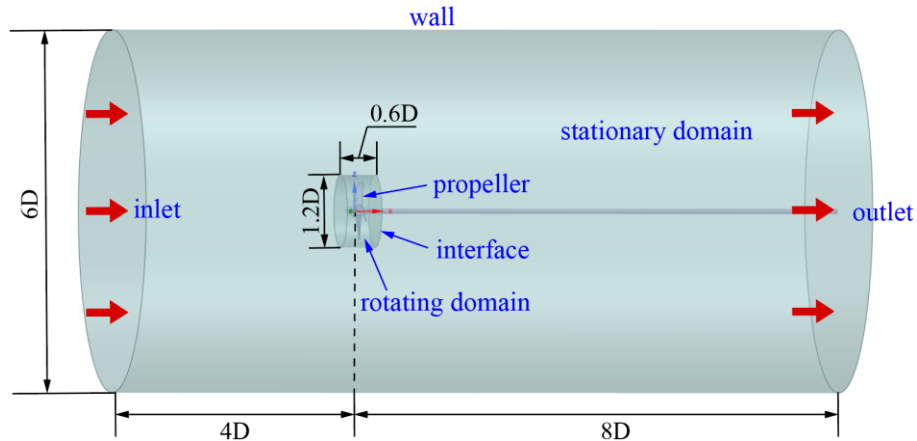


**Fig. 2** Three-dimensional flow field computational region.

After specifying the computational domain, Fluent Meshing is applied to produce the meshes of the rotational region and the static region. Hexahedral structured cells are used to mesh the static region, and unstructured cells are used to mesh the rotational region, as shown in Fig. 3. According to the existing research [22], the hybrid mesh form can reduce the number of meshes and thus improve the computational efficiency.

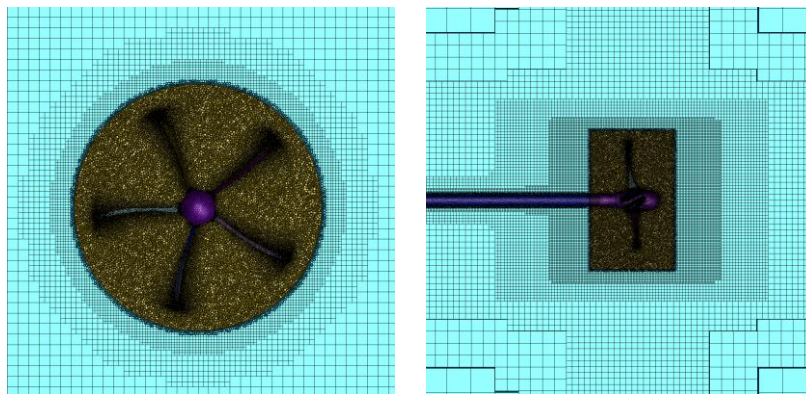


**Fig. 3** Fluid domain computational grid.

ANSYS Fluent is adopted to simulate the hydrodynamic properties of the blade. The turbulence intensity at the velocity inlet is set to 1%. A hydrostatic outlet at 0 Pa reference pressure is used at the outlet boundary. The revolution speed of the internal region is set to 600 RPM. The propeller is simulated as a fluid-structure interface with system coupling motion. The data transfer between the flow field and the structural field is achieved through the system coupling module. The cavitation phenomenon of the propeller is not considered in this study. The temperature of fluid medium water is 25°C with a density of 998kg/m<sup>3</sup>.

### 2.3 Structure model and boundary conditions

The ANSYS ACP module is used to construct a finite element analysis (FEA) model of the composite blade, and the blade arch surface is used as the reference blade surface for the lamination. In this study, only a single composite propeller blade is coupled for calculation. A quadrilateral mesh is used for mesh generation of the reference surface of the pavement to reduce the number of cells and save computational resources. The composite blade adopts the symmetric lay-up method with the propeller arch surface on the suction surface and the pressure surface, which consists of layered solid cells. The layered solid unit could describe the geometric features of the propeller better than other units. The propeller arch surface and FEA model are given in Fig. 4.

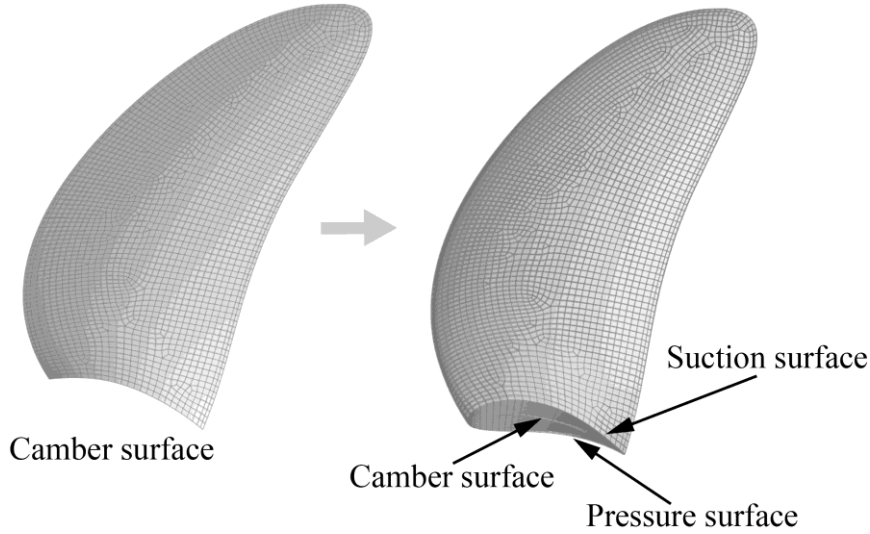


**Fig. 4** FEA model of the composite propeller.

The materials used for the composite lay-up of the propeller and their properties are shown in Table 2. They are manganese aluminum bronze (MAB), epoxy carbon UD (395 Gpa) prepreg (M1), epoxy carbon UD (230 Gpa) prepreg (M2), and epoxy E-glass UD (M3), respectively. Based on previous studies [23], the classical ply thicknesses of composite materials are 0.125 mm, 0.13 mm, and 0.175 mm. Considering that the propeller blade tips are relatively thin, the ply thickness selected for this study is 0.125 mm. Prediction of propeller transient structural response in the ANSYS Transient Structure module. The total simulation time is 0.4 s with a time step of 0.002 s. This is consistent with the settings in the Fluent solver to guarantee that the FSI simulation proceeds smoothly. The centrifugal force of the propeller is realized through a specified rotational speed that is consistent with the rotational domain speed in the fluid domain. The propeller surface is defined as a fluid-solid interface. Fixed support is used at the blade root.

**Table 2** Property of MAB and three different composite materials.

Material	Tensile modulus(MPa)	Shear Modulus (MPa)	Poisson's Ratio	Density (kg/m3)
MAB	1.10E+5	4.10E+4	0.34	8.30E+3
M1	$E_x = 2.09E+5$ $E_y = E_z = 9.45E+3$	$G_{xy} = G_{xz} = 5.50E+3$ $G_{yz} = 3.90E+3$	$V_{xy} = V_{xz} = 0.27$ $V_{yz} = 0.40$	1.54E+3
M2	$E_x = 1.21E+5$ $E_y = E_z = 8.60E+3$	$G_{xy} = G_{xz} = 4.70E+3$ $G_{yz} = 3.10E+3$	$V_{xy} = V_{xz} = 0.27$ $V_{yz} = 0.40$	1.49E+3
M3	$E_x = 4.50E+4$ $E_y = E_z = 1.00E+4$	$G_{xy} = G_{xz} = 5.00E+3$ $G_{yz} = 3.80E+3$	$V_{xy} = V_{xz} = 0.30$ $V_{yz} = 0.40$	2.00E+3

Note: Subscripts  $x$ ,  $y$ , and  $z$  are longitudinal, transverse, and thickness directions of the layered fibers.

## 2.4 Coupling method

The fluid-structure interaction of the blade is essential to consider when analyzing the properties of the propeller, as the interaction between the propeller and the fluid is a dynamic process. In particular, composite blades are more prone to deformation under hydrodynamic loads. The fluid-structure interaction control equation is as follows:

$$[M]\{\ddot{\mu}\} + [C]\{\dot{\mu}\} + [K]\{\mu\} = \{F(t)\} \quad (3)$$

where  $\{u\}$ ,  $\{\dot{u}\}$  and  $\{\ddot{u}\}$  are the displacement vector, velocity vector, and acceleration vector of composite propeller blade nodes, respectively.  $[M]$ ,  $[C]$  and  $[K]$  are the mass matrix, damping matrix, and total stiffness matrix of the structural model respectively. In contrast to the potential flow method, for the CFD method added mass, damping coefficient, and added stiffness coefficient are reflected in the hydrodynamics.  $\{F(t)\}$  represents the total external load, including Coriolis force  $\{F_{co}\}$ , centrifugal force  $\{F_{ce}\}$ , and hydrodynamic force  $\{F_d\}$ , the expressions are as follows:

$$\{F(t)\} = \{F_{co}\} + \{F_{ce}\} + \{F_d\} \quad (4)$$

According to the computational fluid dynamics model and structural model proposed above, the FSI equations of the composite blade are calculated by the CFD/FEM solver Fluent/Transient structural in the ANSYS Workbench platform. The hydrodynamic load and structural deformation of the composite blade are solved under uniform incoming flow. Fig .5 depicts the numerical simulation process for the composite propeller fluid-structure coupling.

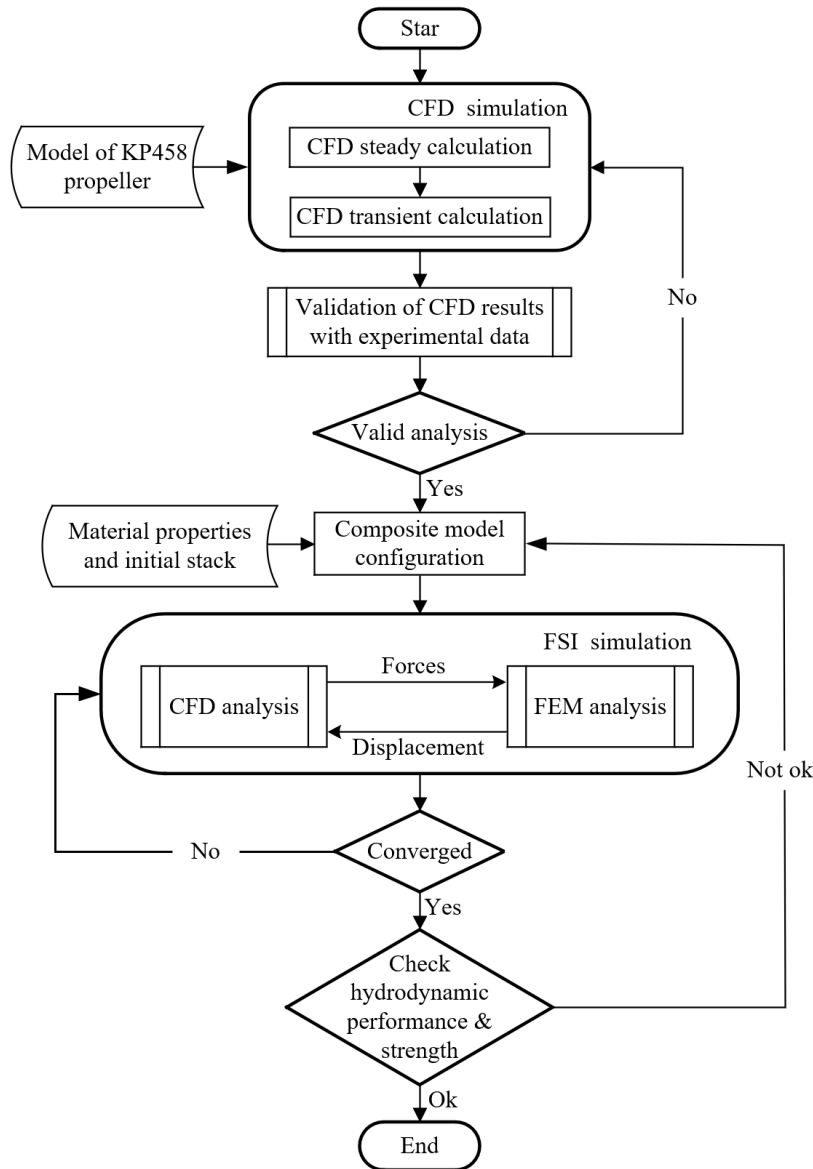


**Fig. 5** Process of the FSI numerical simulation.

## 2.5 Composite failure theories

To verify whether the lay-up entity experiences failure, the FEA model of the blade is assessed by the orthogonal anisotropic Tsai-Wu failure criterion, which is one of the most common and well-established criteria for strength assessment of composite laminates. Where an inverse reserve factor (IRF) above 1 indicates material failure and below 1 indicates material safety. The IRF expression derived from the fiber stress and material properties is as follows:

$$IRF = F_{11}\sigma_1^2 + F_{22}\sigma_2^2 + F_{66}\sigma_6^2 + 2F_{12}\sigma_1\sigma_2 + F_1\sigma_1 + F_2\sigma_2 \quad (5)$$

where  $\sigma_1$  refers to the stress of the thin layer along the fiber direction;  $\sigma_2$  is that stress of the thin layer along the direction perpendicular to the fiber;  $\sigma_6$  is the shear stress resistance of the thin layer;  $F_{ij}$  is the coefficient, which is related to the material strength of the thin layer and can be calculated by the following formula:

$$F_{11} = \frac{1}{X_t X_c} \quad (6)$$

$$F_{22} = \frac{1}{Y_t Y_c} \quad (7)$$

$$F_{66} = \frac{1}{S^2} \quad (8)$$

$$F_1 = \frac{1}{X_t} - \frac{1}{X_c} \quad (9)$$

$$F_2 = \frac{1}{Y_t} - \frac{1}{Y_c} \quad (10)$$

$$F_{12} = -\frac{1}{2}\sqrt{F_{11}F_{22}} \quad (11)$$

where  $X_t$  and  $X_c$  are the tensile and compressive strengths of the thin layer along the fiber direction;  $Y_t$  and  $Y_c$  are the tensile and compressive strength of the thin layer along the direction perpendicular to the fiber;  $S$  is the shear strength of the thin layer along the fiber direction.

## 3. Verification and validation

The hydrodynamic characteristics of a marine propeller are expressed through three dimensionless coefficients, namely, the thrust coefficient  $K_T$ , the torque coefficient  $K_Q$  and the propulsion efficiency  $\eta_0$ . In this paper, based on the ITTC standards [24], they are defined as follows:

$$J = \frac{V_A}{Dn} \quad (12)$$

$$K_T = \frac{T}{\rho n^2 D^4} \quad (13)$$

$$K_Q = \frac{Q}{\rho n^2 D^5} \quad (14)$$

$$\eta_0 = \frac{J \cdot K_T}{2\pi K_Q} \quad (15)$$

where  $T$ ,  $Q$ ,  $D$ ,  $\rho$ ,  $n$ ,  $V_A$ , and  $J$  are the thrust, torque, diameter of the propeller, density of water, propeller rotation speed, advance velocity, and advance ratio, respectively.

### 3.1 Grid convergence verification

The mesh-independence research is conducted to ensure that the numerical simulation results have sufficient accuracy. When  $J = 0.5$ , the thrust coefficient  $K_T$ , torque coefficient  $K_Q$  and efficiency  $\eta_0$  are computed for five different mesh numbers. Table 3 shows the hydrodynamic coefficients of various mesh numbers and the relative error to the experimental values.

**Table 3** The hydrodynamic coefficients at various mesh numbers.

Grid number	$K_T$	$\Delta K_T$	$10K_Q$	$\Delta 10K_Q$	$\eta_0$	$\Delta \eta_0$
0.6million	0.1226	-10.17	0.1687	-1.97	0.5783	-8.37
1.2million	0.1258	-7.83	0.1696	-1.42	0.5901	-6.51
2.2million	0.1306	-4.32	0.1700	-1.24	0.6115	-3.12
3.2million	0.1331	-2.50	0.1702	-1.10	0.6222	-1.42
4.2million	0.1332	—	0.1703	—	0.6223	—

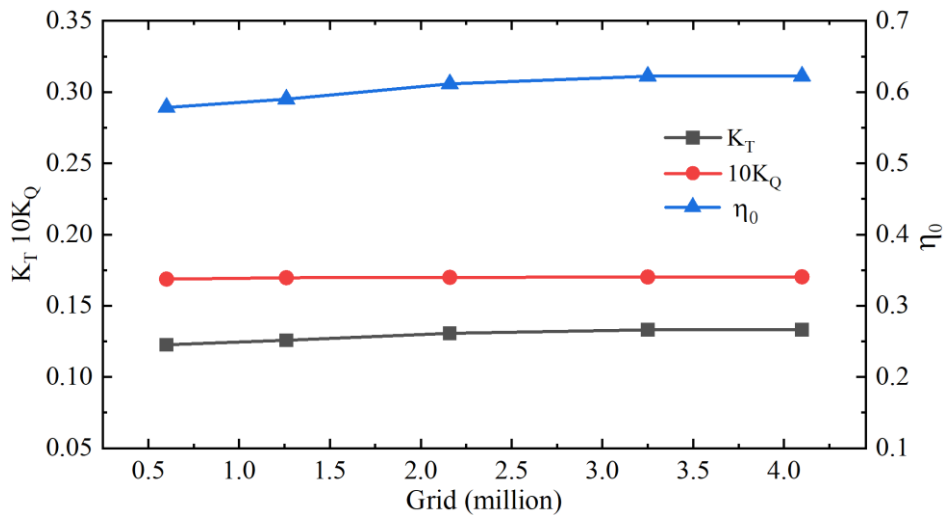


**Fig. 6** Validation of grid convergence ( $J = 0.5$ ).

$$\Delta K_T(\%) = \frac{K_T - K_{T\_Exp}}{K_{T\_Exp}} \times 100 \quad (16)$$

$$\Delta 10K_Q(\%) = \frac{10K_Q - 10K_{Q\_Exp}}{10K_{Q\_Exp}} \times 100 \quad (17)$$

$$\Delta \eta_0(\%) = \frac{\eta_0 - \eta_{0\_Exp}}{\eta_{0\_Exp}} \times 100 \quad (18)$$

The mesh independence studies for five different mesh values of the hydrodynamic coefficients are given in Figure 6. A comparison shows that at  $J = 0.5$ , 3.2 million grids have virtually the equivalent calculated result as 4.2 million grids. Considering the computational cost, efficiency, and accuracy of the simulation for both grid quantities, 3.2 million grids are selected for subsequent calculations.

### 3.2 Adaptability analysis of turbulence model

Turbulence models need to be introduced to close the RANS equations when dealing with Reynolds stress terms. Three turbulence models, RNG  $K - \varepsilon$ , SST  $K - \omega$ , and Reynolds Stress Model (RSM), are selected for turbulence adaptation analysis. The numerical hydrodynamic results of the three different turbulence models for the advance ratio  $J = 0.5$  are given in Fig. 7. The values of  $K_T$  and  $K_Q$  calculated using the SST  $K - \omega$  turbulence model are the closest to the experimental values for open water. As a result, the SST  $K - \omega$  turbulence model is selected for numerical simulation in this paper.

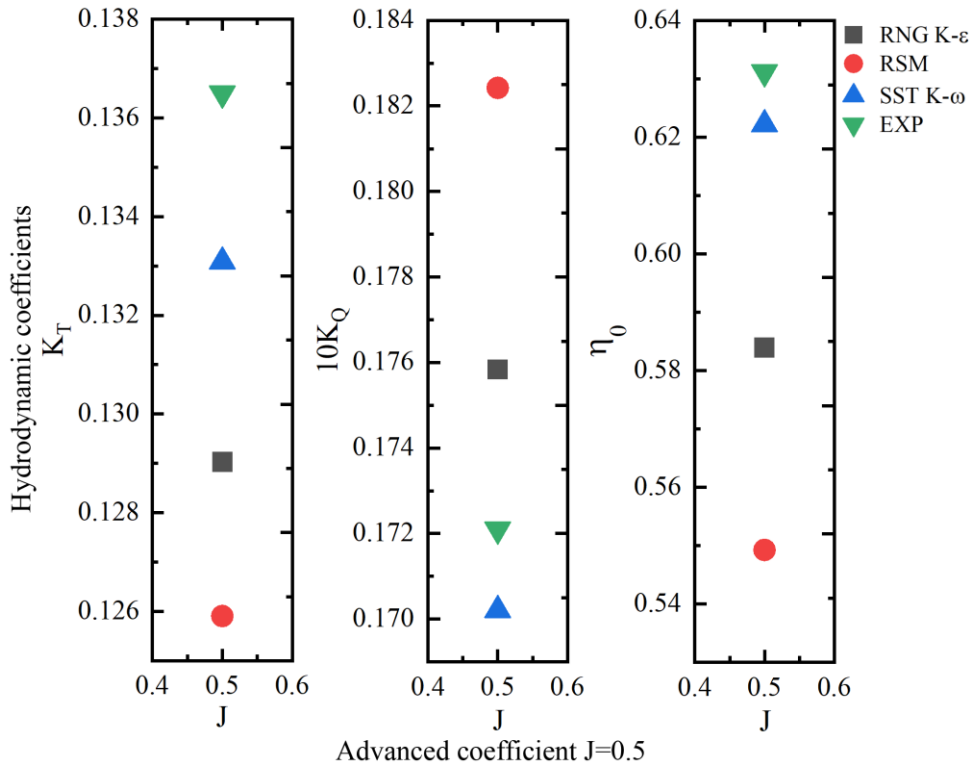


Fig. 7 Hydrodynamic coefficients for various turbulence models ( $J = 0.5$ ).

After numerical simulations of the propeller fluid-solid coupling are carried out, the results of the numerical hydrodynamic calculations of the metal propeller are compared with

the published experimental data from the NMRI, as shown in Fig. 8. It is obvious that the numerical calculations of the hydrodynamic characteristics of the KP458 propeller are in good agreement with the experimental results. The maximum relative error is less than 4.2%, which shows that the numerical results are reliable.

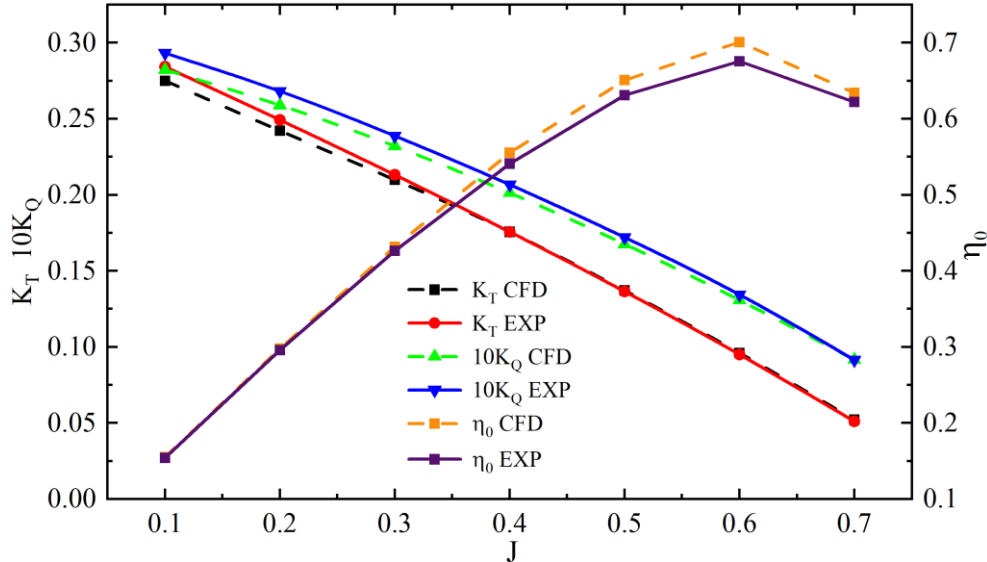


Fig. 8 Comparison of CFD simulation and experimental values of metal propellers.

#### 4. Results and discussion

##### 4.1 Hydrodynamic performance

Since carbon fibre/glass fibre reinforced polymers are widely applied in marine composite propellers, the paper uses this composite material for numerical simulations. The respective polar characteristics of the different composites are given in Fig. 9. A clear anisotropy can be observed with an orthogonal distribution of single-ply tensile and shear stiffnesses.

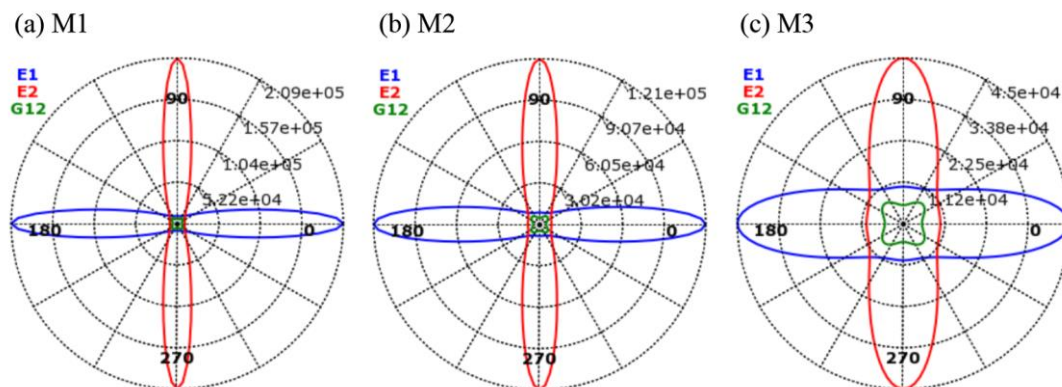


Fig. 9 Polarity properties of different composites.

Three different lay-up sequences of  $[90/90/45/-45]_s$ ,  $[45/-60/90/-30]_s$ , and  $[0/30/-30/60]_s$  are used to build the propeller blade laminate, which is named "Type 1", "Type 2" and "Type 3" respectively. For various lay-up sequences  $[\theta]_s$ , the symbol "s" indicates symmetry about the propeller arches. Fig. 10 shows the reference orientation and lay-up sequence  $[90/90/45/-45]_s$  of the composite propeller blade. The angle  $\theta$  indicates the direction of

laying of the fibers, measured around the 0-degree reference direction (X-axis), and defines a counter-clockwise rotation as positive and a clockwise rotation as negative.

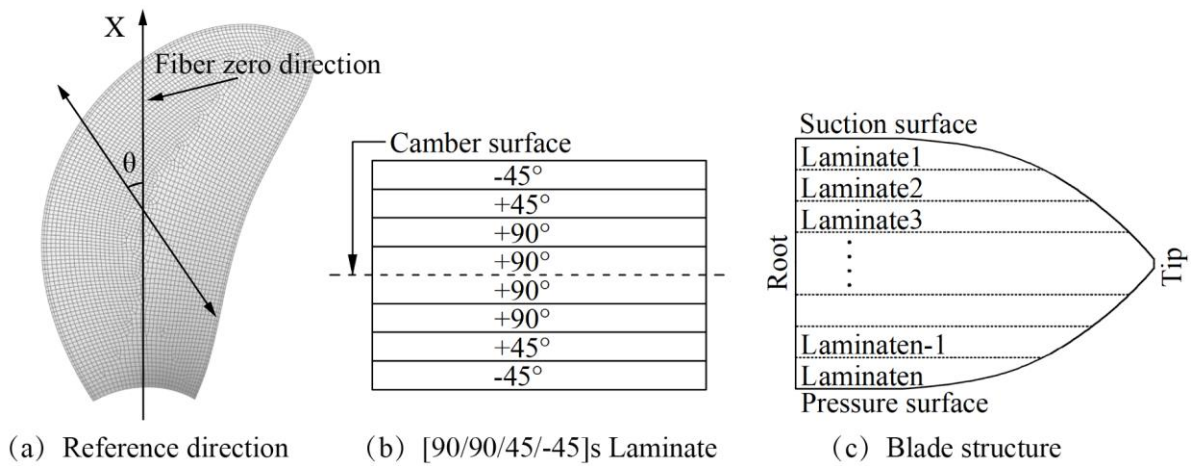


Fig. 10 Lay-up sequence of composite propeller blades.

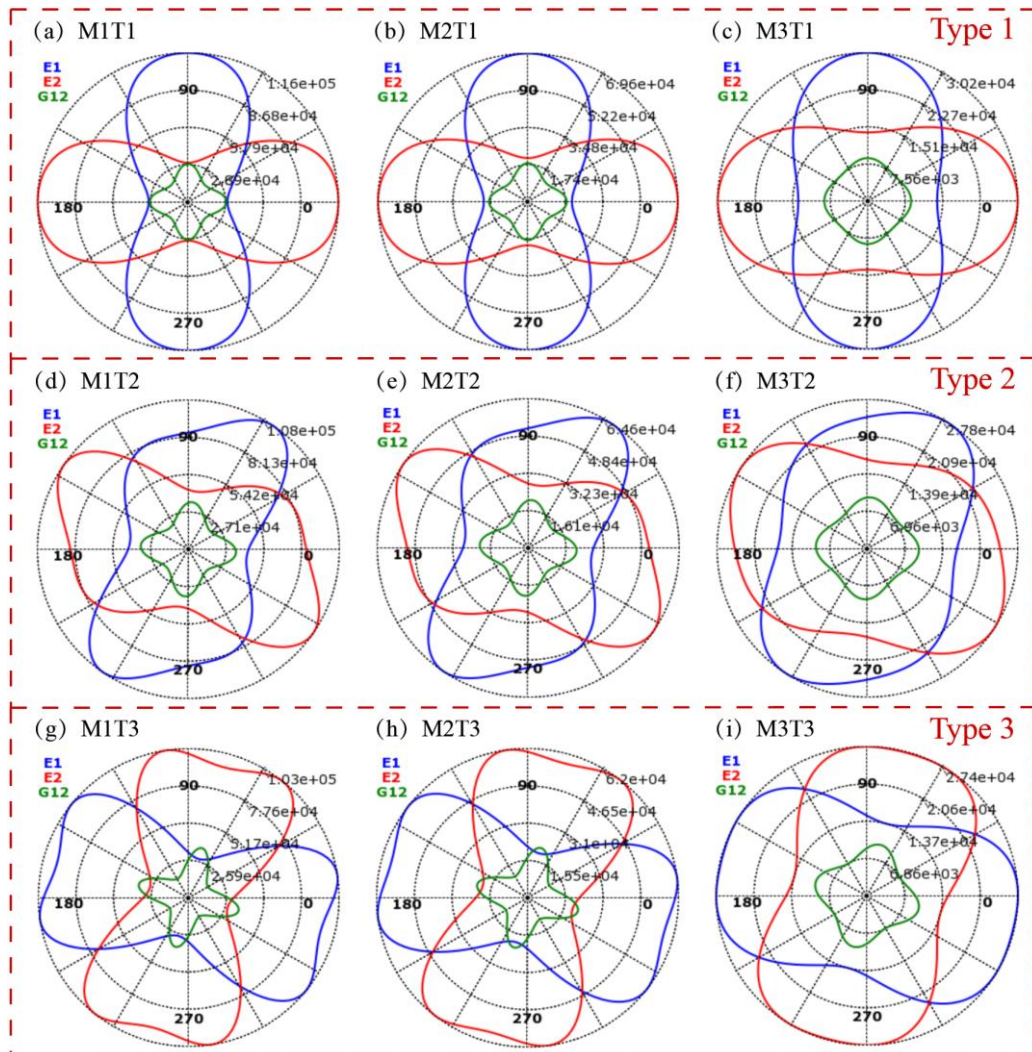


Fig. 11 The polarity characteristics of the various lamination types.

Nine different lamination programs are chosen for numerical analysis for different composites and lay-up orders. Fig. 11 shows The polarity characteristics of the various

lamination types. The combination 'MiTj' denotes the jth layering order of the ith material, illustrated in Table 4.

**Table 4** Lay-up order and materials for different lamination options.

Laminate options	Lay-up order	Material
M1T1	[90/90/45/-45]s	Epoxy carbon UD(395GPa) Prepreg
M2T1	[90/90/45/-45]s	Epoxy carbon UD(230GPa) Prepreg
M3T1	[90/90/45/-45]s	Epoxy E-Glass UD
M1T2	[45/-60/90/-30]s	Epoxy carbon UD(395GPa) Prepreg
M2T2	[45/-60/90/-30]s	Epoxy carbon UD(230GPa) Prepreg
M3T2	[45/-60/90/-30]s	Epoxy E-Glass UD
M1T3	[0/30/-30/60]s	Epoxy carbon UD(395GPa) Prepreg
M2T3	[0/30/-30/60]s	Epoxy carbon UD(230GPa) Prepreg
M3T3	[0/30/-30/60]s	Epoxy E-Glass UD

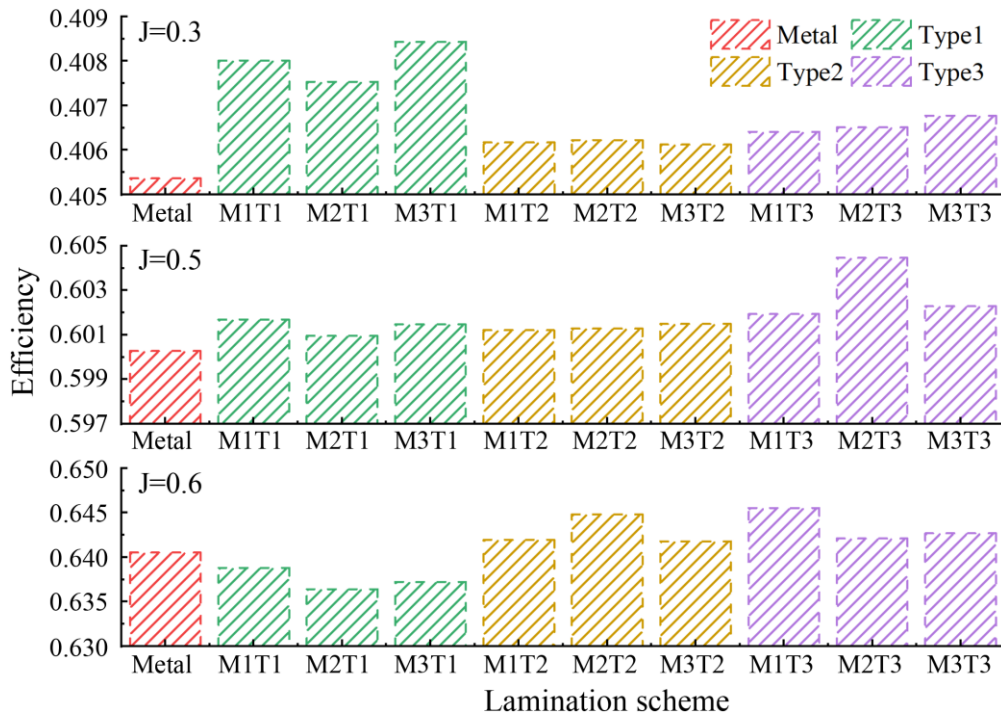


**Fig. 12** Efficiency comparison of composite propellers and metallic ones in various operating situations.

The comparison of the efficiency of metal and composite blades at different operating situations is given in Fig. 12. When  $J = 0.3$ , the composite propeller established by lamination type 1 has the highest propulsion efficiency among the three composites, and the one built by lamination type 2 has the lowest propulsion efficiency. At advance ratio  $J = 0.5$ , the propulsion efficiency of lay-up type 3 is higher than that of type 1 and type 2. The efficiency of all three composite propellers is higher than the metallic blades at  $J = 0.3$  and  $J = 0.5$ . The propulsion efficiency of lay-up type 3 is also significantly better than that of type 1 and type 2 at  $J = 0.6$ , and the efficiency of the metallic propeller is also lower than that of lay-up type 2 and lay-up type 3. Taking into account the comprehensive manifestation of propeller propulsion efficiency in different operating situations, composites M1 and M3 are the best in laminate type 1, while composite M2 works the best in lay-up type 2 and lay-up type 3.

It is observed that the propulsive efficiency of the metallic propeller is lower than the composite ones at both  $J=0.3$  and  $J=0.5$ . It suggests that the new geometrical shape achieved from the deformation of the composite blade under hydrodynamic forces is better than the original metallic blade geometry for the design conditions  $J=0.3$  and  $J=0.5$ .

#### 4.2 Structural performance

The composite propeller's distortion is determined by the hydrodynamic load on the propeller surface and the equivalent stiffness. The greater the equivalent stiffness, the lower the distortion when the hydrodynamic load is equal. The larger the hydrodynamic load, the larger the distortion when the equivalent stiffness is identical.

Fig. 13 shows the maximal distortion of the composite propeller compared with the metallic ones for various lay-up schemes. For lamination type 1 and lamination type 3, the distortion of the composite blade increases gradually with the decrease of Young's modulus under three different operating conditions. For lamination type 2, the distortion of the lamination program M1T2 is larger than that of the lamination program M2T2, although the Young modulus of the composite M2 is smaller than that of the composite M1. This is due to the fact that the equivalent stiffness of the lay-up program M2T2 is greater in the distortion orientation.

The distortion of the propeller built by lamination type 1 is the maximum for the identical material when  $J=0.3$ ,  $J=0.6$ , and  $J=0.8$ . Taking into account the distortion of the propeller in various operating situations, the distortion of the lay-up option M1T3 is the minimum. In addition, the largest distortion of the metallic blade is lower than that of the composite blade. The material M3 with the minimum Young modulus has the maximum distortion for the same lay-up type. The largest distortion of the blade gradually reduces as the advance ratio  $J$  increases.

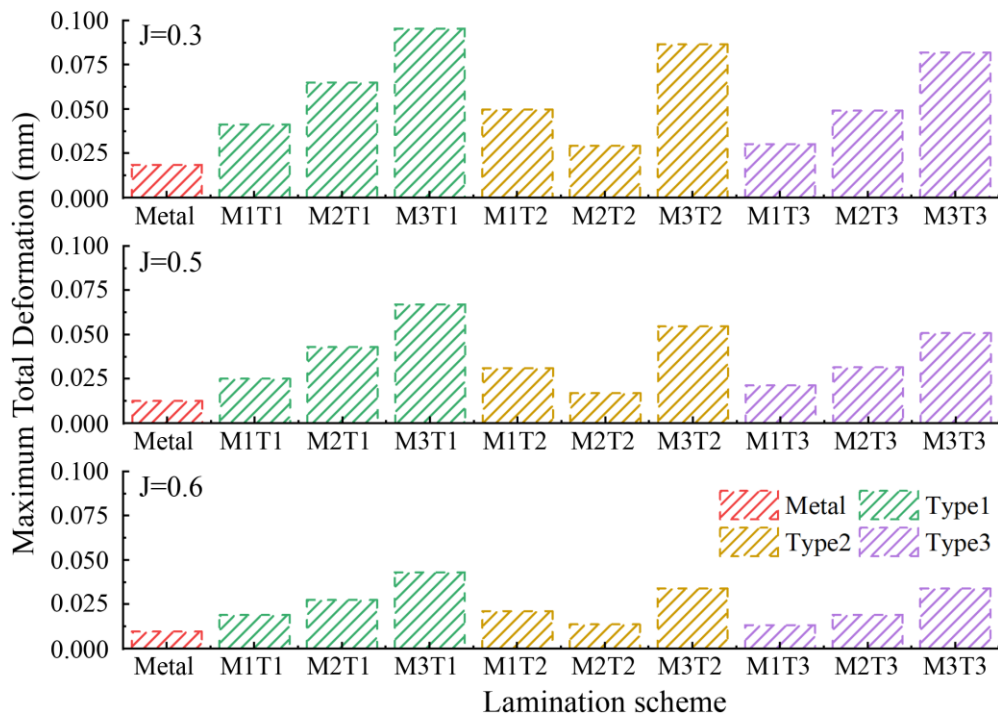


Fig. 13 Comparison of the maximum distortion of composite propellers and metallic ones in various operating situations.

The composite propellers with different lay-up schemes will exhibit different structural responses due to their different equivalent stiffnesses. The deformation contours of the composite propeller are given in Fig. 14. It can be found that the distortion of the composite blade decreases gradually from the tip to the root of the blade, which is distributed in concentric rings, and the maximum distortion occurs at the tip position. The distortion orientation of the propeller blades is different due to the different lay-up materials and lay-up schemes, as shown in Fig. 14. The comparison of Fig. 14(a) and Fig. 14(b) shows that the influence of the layered material on the orientation of blade deformation is greater under the same working situation.

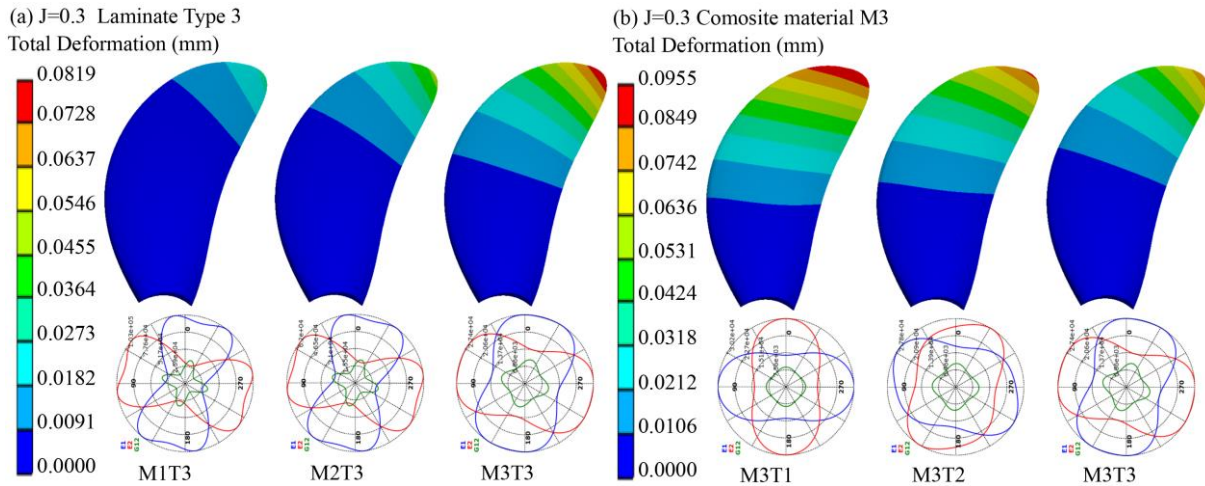


Fig. 14 The total distortion map of the composite blade ; (a) Same lay-up type. (b) Same lay-up material.

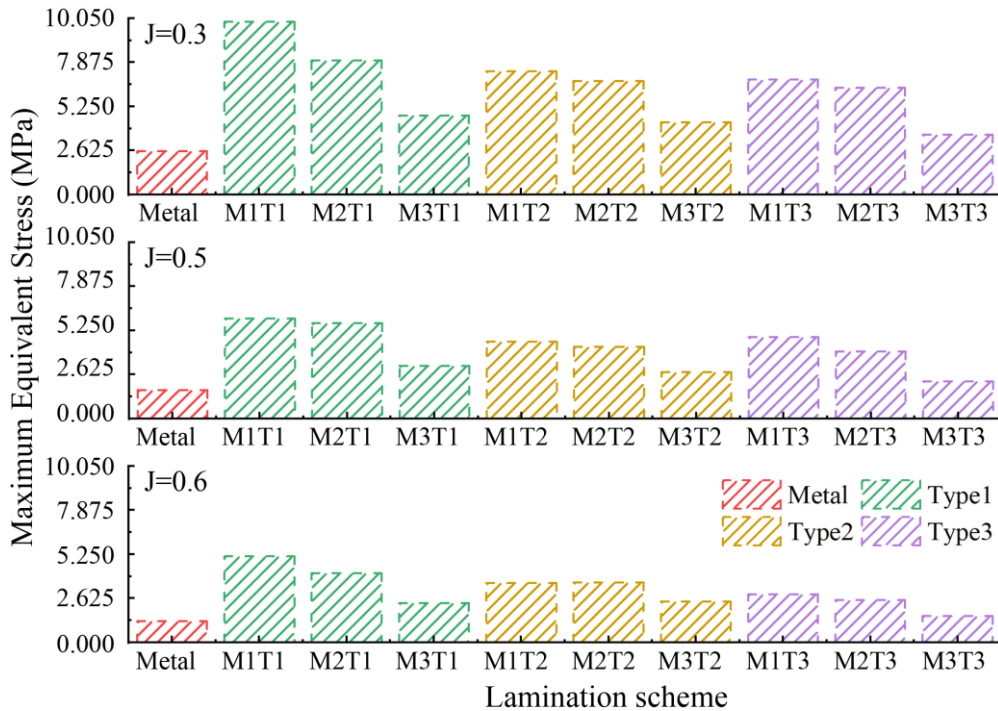
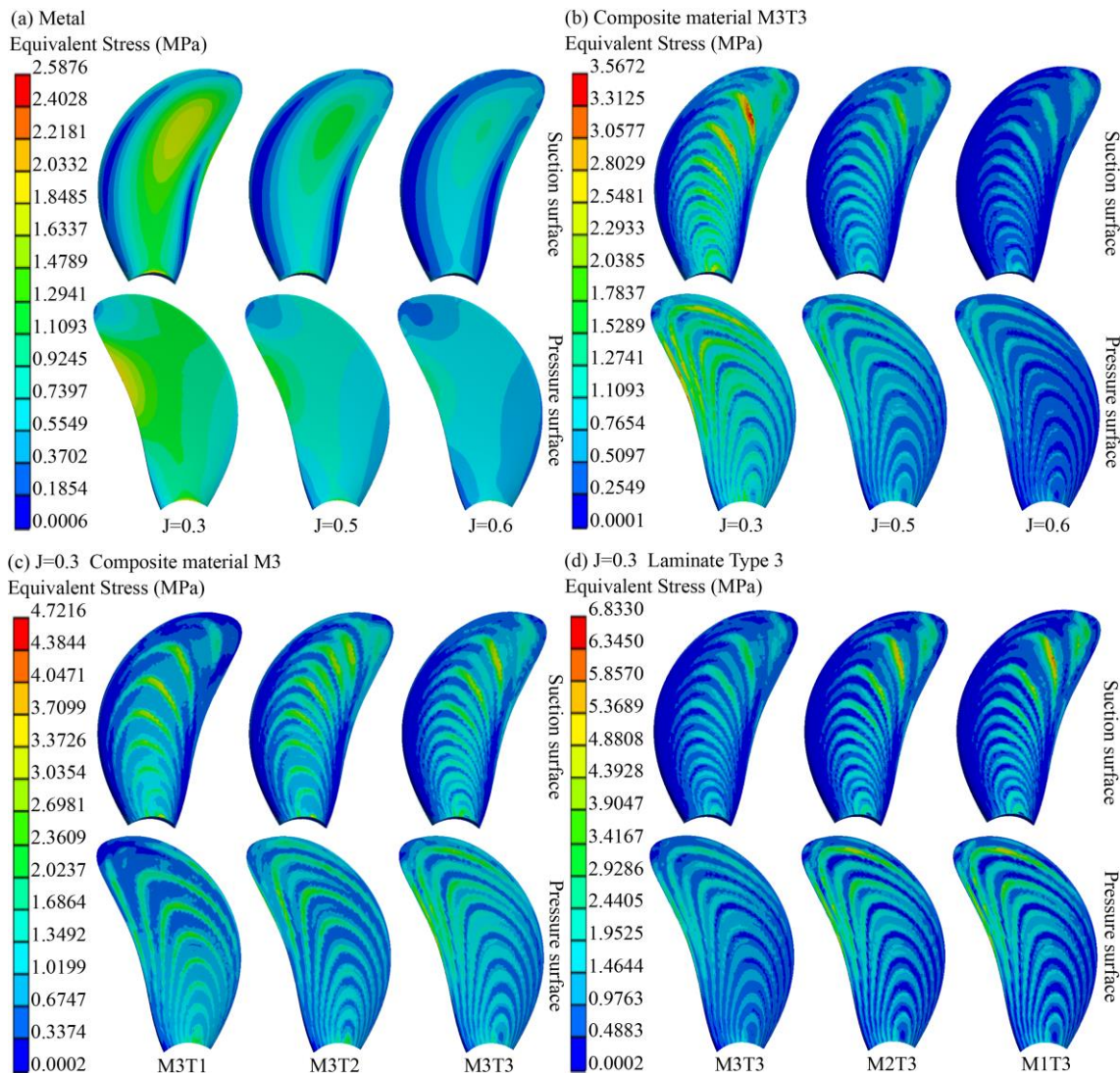


Fig. 15 The comparison of the maximal equivalent stress of metallic blades and composite ones under different operating conditions.

The comparison of the maximum equivalent forces of the metal propeller and the blades with different lay-up types is given in Fig. 15. The maximum equivalent stress of the composite blade with increasing Young's modulus for the same layup type under the same

operating conditions. Namely, the material M1 has the minimum largest equivalent stress for the identical ply type under the same working conditions. For the same ply material in the same condition, ply type 3 has the smallest maximum equivalent stress. In addition, the maximum equivalent stresses of the metallic blades are less than those of the composite blade in identical operating conditions. The maximal equivalent stress between the metallic propeller and the composite ones decreases continuously with increasing  $J$ .

From the analysis in Fig. 15, it can be seen that lay-up type 3, composite material M3, and lay-up scheme M3T3 are of the most concern. The maximum equivalent stress contour plots of composite M3 and ply type 3 with advance ratio  $J = 0.3$  are given in Fig. 16, and the maximum equivalent stress distribution of ply program M3T3 under different operating situations is also shown. It is obvious that the distribution of stresses in the composite blades shows a concentric ring shape, and the stresses are mainly concentrated in the central part of the blades.



**Fig. 16** Equivalent stress contours of the composite propeller; (a) metal propeller (b) composite M3T3 (c)  $J = 0.3$ , composite M3 (d)  $J = 0.3$ , lamination type 3.

The maximal stress of the metal propeller is located at the blade root position in all three operating conditions are shown in Fig. 16(a). The maximum stress of the ply scheme M3T3 is situated in the mid-upper part of the propeller suction side for all three different

operating conditions, as shown in Figure 16(b). The effect of lamination type on stress distribution is shown in Fig. 16(c). At  $J=0.3$ , the lamination scheme M3T3 results in a more uniform stress distribution in the blade compared to the lamination scheme M3T1 and the lamination scheme M3T2. The maximum stresses of pavement type 1 and pavement type 2 are located at the leaf root position, and the maximum stresses of pavement type 3 are located at the middle and upper part of the propeller. The maximal stresses for all three composites of ply type 3 are located in the middle and upper part of the blade suction surface at  $J = 0.3$ , as demonstrated in Fig. 16(d).

### 4.3 Failure criterion

If the inverse reserve factor IRF is greater than or equal to one, the composites are deemed to be destroyed, while the composites are regarded to have sufficient structural strength if the IRF is less than one, in the Tsai-Wu failure principle. The maximum values of IRF corresponding to different lay-up schemes for the three operating conditions are given in Fig. 17.

It can be found that the composite M3 has relatively good strength of the structure in the presence of hydrodynamic loads. In three different operating situations, the IRF values gradually increased for lamination type 1, decreased and then increased for lamination type 2, and decreased for lamination type 3 as Young's modulus of the composite decreased. Taking into account the IRF values under three various operating situations, the composite blade established with M3T3 has a minimal IRF value. In addition, the IRF values of all the lamination schemes in this study are between 0.0081 and 0.0669, which shows that the failure probability of propeller blades under composite lamination is very small and meets the strength requirements.

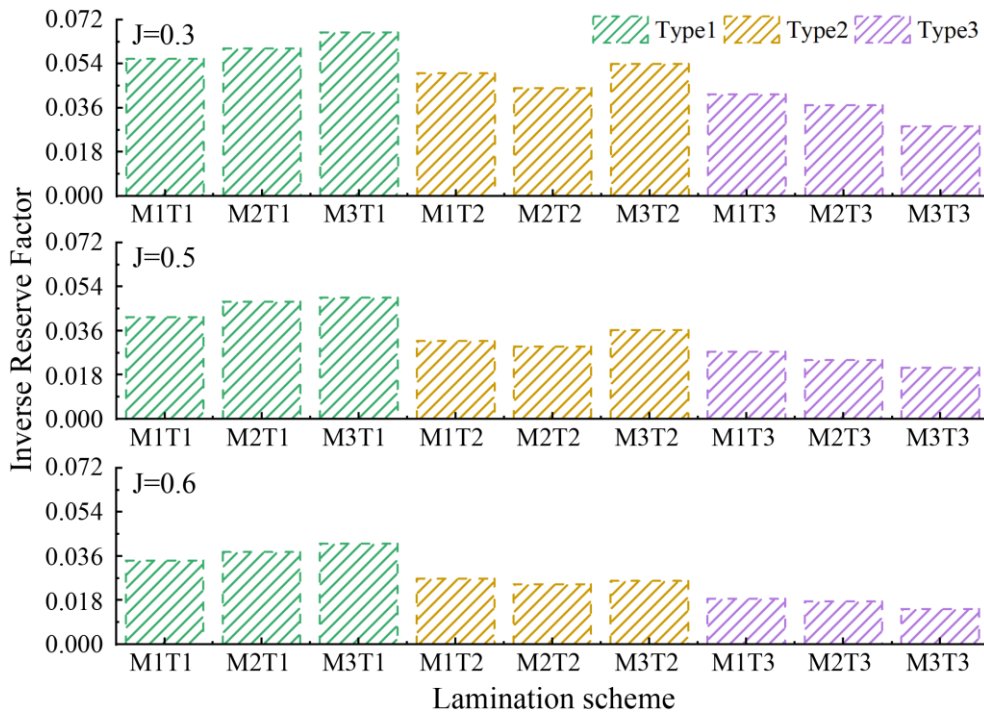


Fig. 17. Maximum value of IRF under different lamination schemes

### 4.4 Parameter optimization

From the above calculations, it is clear that the effects of various ply programs on the properties of composite blades are manifold. For the identical ply program, it could be useful

to improve the hydrodynamic properties of the propeller, but not the structural properties. However, higher efficiency and lower distortion composite propellers are usually required to realize savings and reduce the probability of structural failure [25]. The inverse reserve factors calculated from the various ply programs show that composite propellers completely satisfy the required strength. As a result, the influence of IRF does not need to be considered when the parameters are optimized. Finally, the goal function to assess the total properties of the composite propeller is presented by considering the fluid effects and structural ones, and the expression is as follows:

$$\eta_1 = \frac{1}{m} \sum_{i=1}^m (\eta_{ij} / \eta_i), \quad D_1 = \frac{1}{m} \sum_{i=1}^m (D_{ij} / D_i), \quad G_1 = \frac{\eta_1}{D_1} \quad (18)$$

where  $\eta_i$  and  $D_i$  are the propulsive efficiency and maximum distortion of metal propellers under different working conditions;  $\eta_{ij}$  and  $D_{ij}$  are the propulsive efficiency and maximum distortion of composite propellers under various operating situations and lay-up programs;  $i, j, m$  denote various operating situations, various lay-up programs, and the number of operating situations, accordingly.

The computed results of  $G_1$  for various lay-up planes are given in Fig. 18. The higher the value of this parameter indicates the better total properties of the composite propeller. It is found that when composite M1 is used for blade lay-up design, lay-up type 3 can be selected to build the composite propeller to achieve better performance. When composite M2 is used for blade lay-up design, lay-up type 2 can be selected to build the composite blade to achieve the best properties. For the composite blade in this study, the best lay-up option is M2T2, namely epoxy carbon UD (230 Gpa) prepreg with a lay-up sequence of [45/-60/90/-30]s.

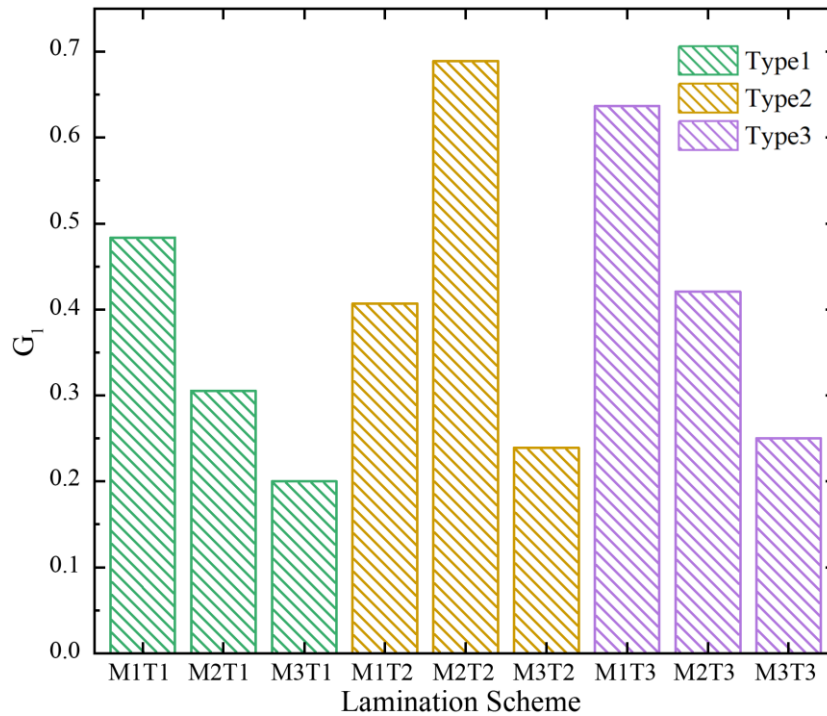


Fig. 18. Optimal values under different lamination schemes

## 5. Conclusion

A computational method for analyzing the transient bidirectional fluid-solid coupling of composite propellers for marine applications is proposed, which is simulated and verified on the metallic propeller. It can forecast its hydrodynamic properties and structural characteristics better. The combined effect of various composites and layup order on propeller performance is given by comparison with metallic propellers. The analysis of this paper leads to the following conclusions:

1. A transient bi-directional fluid-structure coupling algorithm based on the combination of the CFD method and FEM solver applies to the performance forecasting and optimization analysis of marine propellers in the present paper.

2. Taking into account the comprehensive manifestation of propeller propulsion efficiency in various operating situations, composite materials M1 and M3 have the best results in ply type 1. Composites M2 is the finest in ply type 2 and ply type 3. The new geometric shape acquired from the distortion of the composite blade due to hydrodynamic loading is better than the original blade geometry.

3. The lay-up type has a greater influence on the distribution of stresses in the propeller blade, and compared with the lay-up scheme M3T1 and the lay-up scheme M3T2, the lay-up scheme M3T3 makes the distribution of stresses on the blade more uniform. Considering the maximum equivalent stresses in various operating situations, the ply option M3T3 corresponding to the maximum equivalent stresses is the smallest.

4. The IRF values under the three different operating situations are considered comprehensively, and the composite blade established by the lay-up option M3T3 has the lowest IRF value. In addition, the IRF values of all lay-up schemes are in the range of 0.0081 to 0.0669. Namely, the lay-up scheme proposed in this paper is within the safe range.

5. Based on the above conclusions, different composite materials and layup sequences can contribute to alterations in the hydrodynamic and structural performance of the composite propeller. In order to improve the propulsion efficiency and reduce the probability of structural failure, the final optimization is chosen for the lay-up scheme M2T2.

## ACKNOWLEDGEMENT

The authors gratefully acknowledge the support from the National Natural Science Foundation of China (Grant Nos. 51779135 and 51009087) and Shanghai Natural Science Foundation of China (project approval number: 14ZR1419500).

## REFERENCES

- [1] Ekinci, S., 2011. A practical approach for design of marine propellers with systematic propeller series. *Brodogradnja*, 62(2), 123-129.
- [2] Young, Y. L., Motley, M. R., Barber, R., Chae, E. J., Garg, N., 2016. Adaptive Composite Marine Propulsors and Turbines: Progress and Challenges. *Applied Mechanics Reviews*, 68(6), 101-134. <https://doi.org/10.1115/1.4034659>
- [3] Mouritz, A. P., Gellert, E., Burchill, P., Challis, K., 2001. Review of advanced composite structures for naval ships and submarines. *Composite Structures*, 53(1), 21-42. [https://doi.org/10.1016/S0263-8223\(00\)00175-6](https://doi.org/10.1016/S0263-8223(00)00175-6)
- [4] Ghassabzadeh, M., Ghassemi, H., 2013. Determination of hydrodynamics characteristics of marine propeller using hydro-elastic analysis. *Brodogradnja*, 64(1), 40-45.
- [5] Tran, J., Ghazlan, A., Nguyen, T., Gravina, R., 2018. Experimental and theoretical damage assessment in advanced marine composites. *Marine Composites*, 55-84. <https://doi.org/10.1016/B978-0-08-102264-1.00003-0>

- [6] Han, S., Wang, P., Jin, Z., An, X., Xia, H., 2022. Structural design of the composite blades for a marine ducted propeller based on a two-way fluid-structure interaction method. *Ocean Engineering*, 259, 111872. <https://doi.org/10.1016/j.oceaneng.2022.111872>
- [7] Zeng, Z., Yao, Z., Wang, W., Ding, E., 2011. An investigation on performance of composite marine propellers based on Fluid and Structure Interaction. *Journal of Ship Mechanics*, 15(11), 1224-1233. <https://doi.org/10.3969/j.issn.1007-7294.2011.11.005>
- [8] Hussain, M., Abdel, N. Y., Banawan, A., Ahmed, Y. M., 2020. FSI-based structural optimization of thin bladed composite propellers. *Alexandria Engineering Journal*, 59(5), 3755-3766. <https://doi.org/10.1016/j.aej.2020.06.032>
- [9] Young, Y. L., 2008. Fluid-structure interaction analysis of flexible composite marine propellers. *Journal of Fluids and Structures*, 24(6), 799-818. <https://doi.org/10.1016/j.jfluidstructs.2007.12.010>
- [10] Ghassemi, H., Saryazdi, M. G., Ghassabzadeh, M., 2012. Influence of the skew angle on the hydroelastic behaviour of a composite marine propeller. *Journal of Engineering for the Maritime Environment*, 226(4), 346-359. <https://doi.org/10.1177/1475090212440415>
- [11] Lin, H. J., Lin, J. J., Chuang, T. J., 2005. Strength Evaluation of a Composite Marine Propeller Blade. *Journal of Reinforced Plastics and Composites*, 24(17), 1791-1807. <https://doi.org/10.1177/0731684405052199>
- [12] Lin, C., Lee, Y., Hung, C., 2009. Optimization and experiment of composite marine propellers. *Composite Structures*, 89(2), 206-215. <https://doi.org/10.1016/j.compstruct.2008.07.020>
- [13] Das, H. N., Kapuria, S., 2016. On the use of bend-twist coupling in full-scale composite marine propellers for improving hydrodynamic performance. *Journal of Fluids and Structures*, 61, 132-153. <https://doi.org/10.1016/j.jfluidstructs.2015.11.008>
- [14] Lee, H., Song, M., Han, S., Chang, B., Suh, J., 2017. Hydro-elastic aspects of a composite marine propeller in accordance with ply lamination methods. *Journal of Marine Science and Technology*, 22(3), 479-493. <https://doi.org/10.1007/s00773-016-0428-4>
- [15] He, X. D., Hong, Y., Wang, R. G., 2012. Hydroelastic optimisation of a composite marine propeller in a non-uniform wake. *Ocean Engineering*, 39, 14-23. <https://doi.org/10.1016/j.oceaneng.2011.10.007>
- [16] Sun, H. T., Xiong, Y., 2012. Fluid-structure interaction analysis of flexible marine propellers. *Applied Mechanics and Materials*, 226, 479-482. <https://doi.org/10.4028/www.scientific.net/AMM.226-228.479>
- [17] Kumar, A., Vijayakumar, R., Subramanian, V., 2021. Numerical Fluid-Structure Interaction Analysis for a Flexible Marine Propeller Using Co-Simulation Method. *International Journal of Maritime Engineering*, 163, 81-89. <https://doi.org/10.5750/ijme.v163iA2.759>
- [18] Rama, K. V., Sanaka, S. P., Pardhasaradhi, N., Raghava, R. B., 2022. Hydro-elastic computational analysis of a marine propeller using two-way fluid structure interaction. *Journal of Ocean Engineering and Science*, 7(3), 280-291. <https://doi.org/10.1016/j.joes.2021.08.010>
- [19] Soden, P. D., Kaddour, A. S., Hinton, M. J., 2004. Recommendations for designers and researchers resulting from the world-wide failure exercise. *Composites Science and Technology*, 64(3-4), 589-604. [https://doi.org/10.1016/s0266-3538\(03\)00228-8](https://doi.org/10.1016/s0266-3538(03)00228-8)
- [20] Lin, H. J., Lai, W. M., Kuo, Y. M., 2010. Effects of stacking sequence on nonlinear hydroelastic behavior of composite propeller blade. *Journal of Mechanics*, 26(3), 293-298. <https://doi.org/10.1017/S1727719100003841>
- [21] Zhang, X., Hong, Y., Liu, W., Yang, F., Wang, R., 2020. Improving the propulsion performance of composite propellers under off-design conditions. *Applied Ocean Research*, 100, 102164. <https://doi.org/10.1016/j.apor.2020.102164>
- [22] An, X., Wang, P., Song, B., Lessard, L., 2020. Bi-directional fluid-structure interaction for prediction of tip clearance influence on a composite ducted propeller. *Ocean Engineering*, 208, 107390. <https://doi.org/10.1016/j.oceaneng.2020.107390>
- [23] Gay, D., Hoa, S. V., 2007. Composite materials: design and applications. New York, USA, CRC press. <https://doi.org/10.1201/9781420045208>
- [24] Dai, K., Li, Y., Gong, J., Fu, Z., Li, A., Zhang, D., 2022. Numerical study on propulsive factors in regular head and oblique waves. *Brodogradnja*, 73(1), 37-56. <https://doi.org/10.21278/brod73103>
- [25] Zhang, X., Hong, Y., Yang, F., Jiao, W., Wang, R., 2019. Effect of rudder on propulsion performance and structural deformation of composite propellers. *Ocean Engineering*, 182, 318-328. <https://doi.org/10.1016/j.oceaneng.2019.04.075>

Liu Liang, Zhang Baoji, Zhang Hao,  
Tang Hailin, Wang Weijie

Hydrodynamic performance optimization of marine  
propellers based on fluid-structure coupling

Submitted: 22.04.2023.

Liu Liang\*, 3096675628@qq.com  
College of Ocean Science and Engineering, Shanghai Maritime University,  
Shanghai, 201306, China

Accepted: 10.07.2023.

Zhang Baoji, bjzhang@shmtu.edu.cn  
College of Ocean Science and Engineering, Shanghai Maritime University,  
Shanghai, 201306, China

Zhang Hao, haozhang@shmtu.edu.cn  
Merchant Marine College, Shanghai Maritime University,  
Shanghai, 201306, China

Tang Hailin, 649909550@qq.com  
College of Ocean Science and Engineering, Shanghai Maritime University,  
Shanghai, 201306, China

Wang Weijie, ty1822645574@163.com  
Merchant Marine College, Shanghai Maritime University,  
Shanghai, 201306, China